

PAST INSTABILITY OF FLRW SOLUTIONS OF THE EINSTEIN-EULER-SCALAR FIELD EQUATIONS FOR LINEAR EQUATIONS OF STATE $p = K\rho$ WITH $0 \leq K < 1/3$

FLORIAN BEYER, ELLIOT MARSHALL, AND TODD A. OLIYNYK

ABSTRACT. Using numerical methods, we examine, under a Gowdy symmetry assumption, the dynamics of nonlinearly perturbed FLRW fluid solutions of the Einstein-Euler-scalar field equations in the contracting direction for linear equations of state $p = K\rho$ and sound speeds $0 \leq K < 1/3$. This article builds upon the numerical work from [12] in which perturbations of FLRW solutions to the Einstein-Euler equations with positive cosmological constant in the expanding time direction were studied. The numerical results presented here confirm that the instabilities observed in [12, 38] for $1/3 < K < 1$, first conjectured to occur in the expanding direction by Rendall in [42], are also present in the contracting direction over the complementary parameter range $0 \leq K < 1/3$. Our numerical solutions show that the fractional density gradient of the nonlinear perturbations develop steep gradients near a finite number of spatial points and become unbounded towards the big bang. This behaviour, and in particular the characteristic profile of the fractional density gradient near the big bang, is strikingly similar to what was observed in the expanding direction near timelike infinity in the article [12].

1. INTRODUCTION

Perturbed Friedmann-Lemaître-Robertson-Walker (FLRW) spacetimes form the basis of modern cosmology and play a distinguished role in General Relativity. In particular, much research has been devoted to understanding the dynamical behaviour of these spacetimes near big bang singularities. Due to the Hawking-Penrose singularity theorems [28], it is known that cosmological spacetimes without any symmetries are geodesically incomplete to the past (contracting direction) for a large class of matter models. However, it has only been recently established that the past geodesic incompleteness of perturbed Einstein-scalar field FLRW spacetimes, possibly coupled with other matter fields, is due to the formation of quiescent, spacelike big bang singularities where the curvature becomes unbounded [13, 19, 22, 25, 48, 46, 47, 50], which is referred to as *FLRW big bang stability*. More generally, the stability of big bang singularities in the Kasner family of solutions to the Einstein-scalar field equations has been established in [22, 25] for the expected range of quiescent Kasner exponents.

Scalar fields are thought to play an important role during the evolution of the early universe [3, 26]. So, while quiescent big bang singularities are not expected to be generic for most matter models, and indeed this is the view put forward by the BKL conjecture [4, 32], the presence of scalar fields in the early universe imply that quiescent big bang singularities are physically relevant because nonlinear perturbations of FLRW solutions to the Einstein-scalar field system terminate in the past at such singularities. In addition to scalar fields, fluids, and in particular, radiation fluids, must also be considered as matter models of the early universe. First steps in this direction were taken in the articles [47] ($K = 1$ and no scalar field) and [14] ($1/3 < K < 1$), where the stability of FLRW big bang singularities for solutions of the Einstein-Euler-scalar field equations with linear equations of state $p = K\rho$ was established. While these stability results go some way towards understanding the behaviour of fluids near FLRW big bang singularities, they do not apply to radiation fluids $K = 1/3$ or to the case $K < 1/3$. As discussed in [14], see also Section 4.2.1, it is expected that over the range of sound speeds $0 \leq K \leq 1/3$ fluids will behave significantly differently compared to $1/3 < K < 1$.

The aim of this article is to numerically investigate the behaviour towards the past of nonlinear perturbations of FLRW solutions to the Einstein-Euler-scalar field equations for the range of sound speeds $0 \leq K \leq 1/3$. Of particular interest is to resolve the behaviour of the gravitational and matter fields near big bang singularities that form in these perturbed solutions. In order to simplify the problem, we restrict our attention to spatial \mathbb{T}^3 -topologies and numerically solve the Einstein-Euler-scalar field equations under a Gowdy symmetry assumption (see Section 2.1). The advantage of considering Gowdy spacetimes is that the presence of two Killing fields allows us to reduce the Einstein-Euler-scalar field equations to a $(1 + 1)$ -dimensional problem with periodic boundary conditions. This type of simplification has been exploited both analytically and numerically many times in previous studies of the Einstein equations [1, 2, 8, 9, 10, 11, 15, 16, 29, 30, 31, 41, 44].

The numerical simulations we perform reveal that nonlinear Gowdy-symmetric perturbations of FLRW solutions to the Einstein-Euler-scalar field equations display the following behaviour:

- (a) For all sound speeds $K = c_s^2 \in [0, 1]$ and all sufficiently small perturbations of FLRW initial data, a spacelike big bang singularity forms in areal coordinates (see (2.4)) at $\bar{t} = 0$ and the Ricci scalar blows up there.
- (b) For $K \in [0, 1/3)$ and initial data that is sufficiently close to FLRW initial data and for which the spatial velocity vanishes somewhere on the initial hypersurface, the *fractional density gradient* $\frac{\partial \theta \rho}{\rho}$ develops steep gradients and blows up at finitely many spatial points at $\bar{t} = 0$. These blow up points coincide with the vanishing of the spatial velocity at $\bar{t} = 0$. We refer to the sharp features that form near $\bar{t} = 0$ in the fractional density gradient as *spikes*. Moreover, at the spatial points where the spatial fluid velocity vanishes at $\bar{t} = 0$, the fluid behaves asymptotically as $\bar{t} \searrow 0$ like an *orthogonal* fluid, while away from these points it behaves asymptotically like a *tilted* fluid.
- (c) At $K = 1/3$ and for initial data that is sufficiently close to FLRW initial data, we observe no blow-up of the fractional density gradient and it appears that all the (suitably renormalised) fluid and gravitational variables are converging as $\bar{t} \searrow 0$. However, as the blow-up of the fractional density that occurs for $0 \leq K < 1/3$ takes longer and longer to set in as K approaches $1/3$, it could be the case that the perturbations are also unstable for $K = 1/3$ and we are not observing it numerically because we are simply not evolving long enough to see the instability.
- (d) For $K \in (1/3, 1]$ and initial data that is sufficiently close to FLRW initial data, all of the (suitably renormalised) gravitational and matter variables converge at $\bar{t} \searrow 0$ monotonically to limits in accordance with the stability results [14, 47].
- (e) For initial data that is sufficiently far away from FLRW initial data and $K \in [0, 1]$, spikes form in both fluid and metric functions. Intriguingly, the spikes in the fractional density gradient form first and are followed by gravitational spikes that develop in nearly the same location.

These results can be understood by a simple heuristic argument. First suppose that, as the big bang is approached, the dynamics of the Einstein-Euler-scalar field system can be approximated by solutions of the Euler equations on a fixed FLRW-scalar field background and that spatial derivatives are negligible. Then, as we show in Section 4.2.1, the relation

$$\beta(1 - \beta^2)^{-(1-K)/2} = c\bar{t}^{(3K-1)/2} \quad (1.1)$$

holds at each spatial point where c is a constant and the fluid velocity field is determined in terms of β and a natural orthonormal frame $\{e_0, e_1\}$ by

$$v = \frac{e_0 + \beta e_1}{\sqrt{1 - \beta^2}}.$$

The function β , which represents the spatial part of the fluid velocity, takes values in $(-1, 1)$. In particular, (1.1) implies that the asymptotic behaviour of the fluid at each spatial point is determined by the constants c and K . This leads to the following classification of the asymptotic behaviour:

- Orthogonal fluid: $c = 0$, $K \in [0, 1]$.
- Asymptotically orthogonal fluid: $c \neq 0$, $K \in (1/3, 1]$.
- Tilted fluid: $c \neq 0$, $K = 1/3$.
- Asymptotically extremely tilted fluid¹: $c \neq 0$, $K \in [0, 1/3)$.

The instability described above for $K \in [0, 1/3)$ is thus driven by the dramatically different behaviour of the orthogonal and asymptotically extremely tilted fluids.

Interestingly (1.1) also reveals that the opposite dichotomy occurs in the future (expanding) direction corresponding to the limit $\bar{t} \rightarrow \infty$ interchanging the sound speed parameter K range. In fact, FLRW fluid stability for $0 \leq K \leq 1/3$ has been established in [23, 27, 35, 36, 37, 39, 45, 49] and instability for $1/3 < K \leq 1$ in [12, 21]. The FLRW fluid instabilities that were observed numerically in Gowdy-symmetric solutions for $1/3 < K < 1$ in [12] were predicted by Rendall [42] and are driven by the blow-up of the fractional density gradient $\frac{\partial \theta \rho}{\rho}$. Indeed, it was observed in [12] that for all $K \in (1/3, 1)$ and all choices of initial data sufficiently close to FLRW initial data, the fractional density gradient develops steep gradients and blows up at finitely many spatial points at future timelike infinity.² It is also interesting to note that the blow-up profiles of the fractional density gradient near future timelike infinity observed in [12] are remarkably similar to the blow-up profiles of the fractional density gradient near the big bang singularity at $\bar{t} = 0$ in the numerical simulations presented here.

1.1. Prior and related results: The fluid instability described above in points (b) and (e) is referred to as a *tilt-instability* in [33]. In that article and also [17, 18], the authors construct analytic and numerical solutions of the Einstein-Euler equations with a G_2 symmetry³ that exhibit spikes in both the fluid and gravitational

¹A fluid is described as having an ‘extreme tilt’ if the leading order behaviour of the fluid, as the singularity is approached, is a null vector.

²See [40] for a rigorous analysis of this instability in the simplified setting where coupling to Einstein’s equations is ignored.

³ G_2 models include Gowdy spacetimes as a special case, see [34].

fields and are clearly related to what we observe numerically in this article, see point (e) above. In contrast, the stability dichotomy, see points (b)-(d) above, that we observe in this article for sufficiently small perturbations of FLRW solutions of the Einstein-Euler-scalar field equations is new, as is the clear characterisation of the fluid instability for $0 \leq K < 1/3$ as blow-up of the fractional density gradient $\frac{\partial_\theta \rho}{\rho}$ at the big bang singularity located at $\bar{t} = 0$ and the identification of the fluid spikes as large gradients that develop in the fractional density gradient near $\bar{t} = 0$. It would be interesting to understand if a similar behaviour occurs for small perturbations of the Kasner family of solutions to the Einstein-Euler-scalar fields equations for all exponents that lie in the quiescent range.

1.2. Overview: The article is organised as follows: the derivation of a first order formulation of the Gowdy-symmetric Einstein-Euler-scalar field equations that is suitable for numerical implementation and constructing solutions globally to the future is carried out in Section 2. In Section 3, we derive the FLRW background solutions that we perturb and in Section 4 we discuss our numerical setup and results for small perturbations of the FLRW solution. Finally, in Section 5 we investigate large perturbations and the interactions between gravitational spikes and spikes in the fractional density gradient.

2. EINSTEIN-EULER-SCALAR FIELD EQUATIONS

2.1. Einstein-Euler-scalar field equations with Gowdy symmetry. The Einstein-Euler-scalar field equations⁴ for a perfect fluid and minimally-coupled scalar field are given by⁵

$$G_{ij} = T_{ij}^{\text{fl}} + T_{ij}^{\phi}, \quad (2.1)$$

$$\nabla^i T_{ij}^{\text{fl}} = 0, \quad (2.2)$$

$$\nabla^i T_{ij}^{\phi} = 0, \quad (2.3)$$

where

$$T_{ij}^{\phi} = \nabla_i \phi \nabla_j \phi - \frac{1}{2} g_{ij} \nabla^a \phi \nabla_a \phi$$

is the scalar field stress-energy tensor and

$$T_{ij}^{\text{fl}} = (\rho + p) v_i v_j + p g_{ij}$$

is the perfect fluid stress-energy tensor. Here, v_i is the fluid four-velocity normalised by $v_i v^i = -1$, and we assume that the fluid's proper energy density, ρ , and pressure, p , are related via the linear equation of state

$$p = K \rho,$$

where the constant parameter $K \geq 0$ is the square of the sound speed. In the following, we assume that $0 \leq K \leq 1$ so that the speed of sound is less than or equal to the speed of light.

As discussed in the introduction, we restrict our attention to solutions of the Einstein-Euler-scalar field equations with a Gowdy symmetry [16, 24] by considering Gowdy metrics in areal coordinates on $\mathbb{R}_{>0} \times \mathbb{T}^3$ of the form

$$g = e^{2(\eta-U)} (-e^{2\bar{\alpha}} d\bar{t} \otimes d\bar{t} + d\theta \otimes d\theta) + e^{2U} (dy + Adz) \otimes (dy + Adz) + e^{-2U} \bar{t}^2 dz \otimes dz. \quad (2.4)$$

Here, the functions η , U , $\bar{\alpha}$, and A depend only on $(\bar{t}, \theta) \in \mathbb{R}_{>0} \times \mathbb{R}$ and are 2π -periodic in θ . Since our spatial slices are \mathbb{T}^3 , the metric is periodic and compact in y and z as well, however, these coordinates play no role due to the symmetry condition. For an in-depth discussion of spacetimes with $U(1) \times U(1)$ symmetry and compact spatial slices see [16]. Following previous numerical studies of the initial singularity in Gowdy symmetry [6, 7, 8], we introduce a new time t and metric function α via

$$\bar{t} = e^{-t}, \quad \bar{\alpha} = \alpha + t, \quad (2.5)$$

which allows us to express the Gowdy metric (2.4) as

$$g = e^{2(\eta-U)} (-e^{2\alpha} dt \otimes dt + d\theta \otimes d\theta) + e^{2U} (dy + Adz) \otimes (dy + Adz) + e^{-2U-2t} dz \otimes dz, \quad (2.6)$$

where the big bang singularity is now located at $t = \infty$. We are only interested in solutions in the contracting direction, i.e. towards the past, and consequently, we consider time intervals of the form $t \in [t_0, \infty)$ for some $t_0 \in \mathbb{R}$.

Next, we turn to expressing the Einstein-Euler-scalar field system (2.1)-(2.3) in a Gowdy-symmetric form suitable for numerical implementation. This involves expressing the Einstein and scalar field equations in first

⁴Our indexing conventions are as follows: lower case Latin letters, e.g. i, j, k , will label spacetime coordinate indices that run from 0 to 3 while upper case Latin letters, e.g. I, J, K , will label spatial coordinate indices that run from 1 to 3.

⁵Here, we use units where $c = 1$ and $G = \frac{1}{8\pi}$.

order form and choosing appropriate variables to formulate the Euler equations. The details of the derivation are presented in the following three sections.

2.2. A First Order Formulation of the Einstein Equations. In Gowdy symmetry, the fluid four-velocity only has two non-zero components⁶ and can be expressed as

$$v = v_0 dt + v_1 d\theta, \quad (2.7)$$

where the functions v_0 and v_1 depend on $(t, \theta) \in \mathbb{R} \times \mathbb{R}$ and are 2π -periodic in θ . Due to the normalisation $v_i v^i = -1$, only one of these functions are independent and we take v_1 as our primary fluid velocity variable. Furthermore, the scalar field in Gowdy symmetry also depends on $(t, \theta) \in \mathbb{R} \times \mathbb{R}$ and is 2π -periodic in θ . With these choices, the non-zero components of the total stress-energy tensor

$$T_{ij} = T_{ij}^{\text{fl}} + T_{ij}^{\phi}$$

are given by

$$\begin{aligned} T_{00} &= -e^{2(\alpha+\eta-U)} K\rho + (1+K)\rho v_0^2 + (\partial_t \phi)^2 + \frac{1}{2}e^{2(\alpha+\eta-U)} \left(e^{2(U-\eta)} (\partial_\theta \phi)^2 - e^{-2(\alpha+\eta-U)} (\partial_t \phi)^2 \right), \\ T_{01} &= (1+K)\rho v_0 v_1 + \partial_t \phi \partial_\theta \phi, \\ T_{11} &= e^{2(\eta-U)} K\rho + (1+K)\rho v_1^2 + (\partial_\theta \phi)^2 - \frac{1}{2}e^{2(\eta-U)} \left(e^{2(U-\eta)} (\partial_\theta \phi)^2 - e^{-2(\alpha+\eta-U)} (\partial_t \phi)^2 \right), \\ T_{22} &= e^{2U} K\rho - \frac{1}{2}e^{2U} \left(e^{2(U-\eta)} (\partial_\theta \phi)^2 - e^{-2(-U+\alpha+\eta)} (\partial_t \phi)^2 \right), \\ T_{23} &= e^{2U} K\rho A - \frac{1}{2}e^{2U} A \left(e^{2(U-\eta)} (\partial_\theta \phi)^2 - e^{-2(\alpha+\eta-U)} (\partial_t \phi)^2 \right), \\ T_{33} &= (e^{2U} A^2 + e^{-2U-2t}) \left(K\rho - \frac{1}{2} \left(e^{2(U-\eta)} (\partial_\theta \phi)^2 - e^{-2(\alpha+\eta-U)} (\partial_t \phi)^2 \right) \right). \end{aligned}$$

Using these expressions and the Gowdy metric (2.6), a straightforward calculation shows that the Einstein equation (2.1) in Gowdy symmetry consists of following three wave equations

$$\partial_{tt} A = e^{2\alpha} \left(\partial_\theta A (4\partial_\theta U + \partial_\theta \alpha) + \partial_{\theta\theta} A \right) + \partial_t A (-1 - 4\partial_t U + \partial_t \alpha), \quad (2.8)$$

$$\partial_{tt} U = \frac{1}{2} + \frac{1}{2}e^{2t+4U} \left((\partial_t A)^2 - e^{2\alpha} (\partial_\theta A)^2 \right) + e^{2\alpha} \partial_\theta U \partial_\theta \alpha + e^{2\alpha} \partial_{\theta\theta} U + \partial_t U + \frac{1}{2} \partial_t \alpha + \partial_t U \partial_t \alpha, \quad (2.9)$$

$$\begin{aligned} \partial_{tt} \eta &= -\frac{1}{4}e^{-2U} \left(4e^{2\alpha+2\eta} K\rho + e^{2t+6U+2\alpha} (\partial_\theta A)^2 - 4e^{2U+2\alpha} (\partial_\theta U)^2 - 4e^{2U+2\alpha} (\partial_\theta \alpha)^2 \right. \\ &\quad - 4e^{2U+2\alpha} \partial_\theta \alpha \partial_\theta \eta - 2e^{2U+2\alpha} (\partial_\theta \phi)^2 - 4e^{2U+2\alpha} \partial_{\theta\theta} \alpha \\ &\quad \left. - 4e^{2U} (\partial_t U)^2 - 4e^{2U} \partial_t \alpha \partial_t \eta + 2e^{2U} (\partial_t \phi)^2 \right), \end{aligned} \quad (2.10)$$

and three first order equations

$$\partial_t \alpha = -1 - 2e^{2(\alpha+\eta-U)} K\rho + (1+K)\rho v_0^2 - e^{2\alpha}(1+K)\rho v_1^2, \quad (2.11)$$

$$\begin{aligned} \partial_t \eta &= -\frac{1}{4}e^{-2U} \left(-4e^{2(\alpha+\eta)} K\rho + 4e^{2U} \rho v_0^2 + 4e^{2U} K\rho v_0^2 + e^{2t+6U+2\alpha} (\partial_\theta A)^2 + 4e^{2(U+\alpha)} (\partial_\theta U)^2 \right. \\ &\quad \left. + 2e^{2U+2\alpha} (\partial_\theta \phi)^2 + e^{2t+6U} (\partial_t A)^2 + 4e^{2U} (\partial_t U)^2 + 2e^{2U} (\partial_t \phi)^2 \right), \end{aligned} \quad (2.12)$$

$$\partial_\theta \eta = \frac{1}{2} \left(-2\rho v_0 v_1 - 2K\rho v_0 v_1 - 2\partial_\theta \alpha - e^{2t+4U} \partial_\theta A \partial_t A - 4\partial_\theta U \partial_t U - 2\partial_\theta \phi \partial_t \phi \right), \quad (2.13)$$

where we note that (2.12) and (2.13) are the Hamiltonian and momentum constraints, respectively.

Either of (2.10) or (2.12) can be used to evolve the metric variable η . Following our previous numerical study of the Gowdy-symmetric Einstein-Euler equations in the expanding direction [12], we use (2.12) to evolve η . This choice, as discussed in [12], has the benefit of enforcing the Hamiltonian constraint⁷ at every time step and involves solving a first order equation for η rather than a second order one. Moreover, because we use (2.12) to evolve η , we can view (2.10) as a constraint equation that can be used to verify our numerical results.

Next, introducing the first order variables

$$A_0 = \partial_t A, \quad A_1 = e^\alpha \partial_\theta A, \quad U_0 = \partial_t U, \quad U_1 = e^\alpha \partial_\theta U, \quad (2.14)$$

⁶This follows from choosing coordinates where the two Killing vectors are given by ∂_y and ∂_z , see [31].

⁷The importance of enforcing the Hamiltonian constraint for numerical simulations is further discussed in [5].

we can express the wave equations (2.8)-(2.9) for A and U in first order form as

$$\partial_t \begin{pmatrix} A_0 \\ A_1 \end{pmatrix} + \begin{pmatrix} 0 & -e^\alpha \\ -e^\alpha & 0 \end{pmatrix} \partial_\theta \begin{pmatrix} A_0 \\ A_1 \end{pmatrix} - \alpha_0 \begin{pmatrix} A_0 \\ A_1 \end{pmatrix} = \begin{pmatrix} -A_0 - 4A_0U_0 + 4A_1U_1 \\ 0 \end{pmatrix}, \quad (2.15)$$

$$\partial_t \begin{pmatrix} U_0 \\ U_1 \end{pmatrix} + \begin{pmatrix} 0 & -e^\alpha \\ -e^\alpha & 0 \end{pmatrix} \partial_\theta \begin{pmatrix} U_0 \\ U_1 \end{pmatrix} - \alpha_0 \begin{pmatrix} U_0 \\ U_1 \end{pmatrix} = \begin{pmatrix} \frac{1}{2} + \frac{1}{2}e^{4U+2t}(A_0^2 - A_1^2) + U_0 + \frac{1}{2}\alpha_0 \\ 0 \end{pmatrix}. \quad (2.16)$$

2.3. A First Order Formulation of the Scalar Field Equation. The equation of motion (2.3) for the scalar field is equivalent to the wave equation $g^{ab}\nabla_a\nabla_b\phi = 0$ which, using the Gowdy metric (2.6), can be expressed as

$$\partial_{tt}\phi = (e^{2\alpha}\partial_\theta\alpha\partial_\theta\phi + e^{2\alpha}\partial_\theta\partial_\theta\phi + \partial_t\phi + \partial_t\phi\partial_t\alpha).$$

Introducing the variables

$$\phi_0 = \partial_t\phi, \quad \phi_1 = e^\alpha\partial_\theta\phi, \quad (2.17)$$

allows us to write the scalar field equation in the first order form as

$$\partial_t \begin{pmatrix} \phi_0 \\ \phi_1 \end{pmatrix} + \begin{pmatrix} 0 & -e^\alpha \\ -e^\alpha & 0 \end{pmatrix} \partial_\theta \begin{pmatrix} \phi_0 \\ \phi_1 \end{pmatrix} - \alpha_0 \begin{pmatrix} \phi_0 \\ \phi_1 \end{pmatrix} = \begin{pmatrix} \phi_0 \\ 0 \end{pmatrix}. \quad (2.18)$$

2.4. Euler Equations. Following [12], the Euler equations (2.2) can be expressed in Gowdy symmetry as

$$B^0\partial_0V + B^1\partial_1V = F, \quad (2.19)$$

where

$$V = \begin{pmatrix} \rho \\ v_1 \end{pmatrix},$$

$$B^0 = \begin{pmatrix} \frac{K}{\rho+K\rho} (g_{11} + (v_1)^2) & Kv_1 \\ Kv_1 & \rho + K\rho \end{pmatrix},$$

$$B^1 = (-v_0) \begin{pmatrix} \frac{K}{\rho+K\rho} v_1 & K \\ K & (\rho + K\rho) \frac{v_1}{g_{11} + (v_1)^2} \end{pmatrix},$$

and

$$F = \frac{1}{2}(-v_0) \begin{pmatrix} K(2g^{11}\partial_1g_{11} - g^{ab}\partial_1g_{ab})v_1 \\ (\rho + K\rho) \left(\frac{(v_1)^2}{g_{11} + (v_1)^2} g^{11}\partial_1g_{11} - g^{00}\partial_1g_{00} \right) \end{pmatrix} + \frac{K}{2} \begin{pmatrix} (v_1)^2 g^{11}\partial_0g_{11} - (g_{11} + (v_1)^2)g^{IK}\partial_0g_{IK} \\ 0 \end{pmatrix}.$$

To facilitate the study of the fluid near the big bang singularity, which is now located at $t = \infty$, we remove the leading order behaviour in t from the fluid density ρ by employing a renormalised density $\tilde{\rho}$ defined by

$$\rho = e^{\frac{3(1+K)}{2}t} \tilde{\rho}. \quad (2.20)$$

Next, we differentiate (ρ, v_1) to obtain the identities

$$\partial_t \begin{pmatrix} \rho \\ v_1 \end{pmatrix} = P\partial_t \begin{pmatrix} \tilde{\rho} \\ v_1 \end{pmatrix} + Z \quad \text{and} \quad \partial_\theta \begin{pmatrix} \rho \\ v_1 \end{pmatrix} = P\partial_\theta \begin{pmatrix} \tilde{\rho} \\ v_1 \end{pmatrix},$$

where

$$P = \begin{pmatrix} e^{\frac{3(1+K)}{2}t} & 0 \\ 0 & 1 \end{pmatrix} \quad \text{and} \quad Z = \begin{pmatrix} \frac{3(1+K)}{2}e^{\frac{3(1+K)}{2}t}\tilde{\rho} \\ 0 \end{pmatrix}.$$

Using these identities, we can express the Euler equations (2.19) as

$$\tilde{B}^0\partial_t\tilde{\mathbf{V}} + \tilde{B}^1\partial_\theta\tilde{\mathbf{V}} = F_{\tilde{\mathbf{V}}}, \quad (2.21)$$

where

$$\tilde{\mathbf{V}} = (\tilde{\rho}, v_1)^T$$

and $\tilde{B}^0 := P^T B^0 P$, $\tilde{B}^1 := P^T B^1 P$ and $F_{\tilde{\mathbf{V}}} := P^T(F - B^0 Z)$ take the form

$$\tilde{B}^0 = \begin{pmatrix} \frac{K(e^{2\eta} + e^{2U}(v_1)^2)}{e^{2U}(1+K)\tilde{\rho}} & Kv_1 \\ Kv_1 & (1+K)\tilde{\rho} \end{pmatrix},$$

$$\tilde{B}^1 = \begin{pmatrix} -\frac{Kv_1(e^{2\alpha}(e^{-2U+2\eta} + (v_1)^2))^{1/2}}{(1+K)\tilde{\rho}} & -K(e^{2\alpha}(e^{-2U+2\eta} + (v_1)^2))^{1/2} \\ -K(e^{2\alpha}(e^{-2U+2\eta} + (v_1)^2))^{1/2} & -\frac{e^{2\alpha}(1+K)\tilde{\rho}v_1}{(e^{2\alpha}(e^{-2U+2\eta} + (v_1)^2))^{1/2}} \end{pmatrix}$$

and

$$F_{\tilde{\mathbf{V}}} = \left(\begin{array}{c} -\frac{K(e^{2U}(v_1)^2 - 2e^{2U}v_1(e^{2\alpha}(e^{-2U+2\eta} + (v_1)^2))^{1/2}\partial_\theta\alpha + e^{2\eta}(1-2\partial_t U + 2\partial_t\eta))}{\frac{1}{2}(1+K)\tilde{\rho}(-3Kv_1 + \frac{2(e^{2\alpha}(e^{-2U+2\eta} + (v_1)^2))^{1/2}(e^{2U}(v_1)^2\partial_\theta\alpha + e^{2\eta}(-\partial_\theta U + \partial_\theta\alpha + \partial_\theta\eta))}{e^{2\eta} + e^{2U}(v_1)^2})} \end{array} \right),$$

respectively.

2.5. The Complete Evolution System. Combining (2.11), (2.12), (2.15), (2.16), (2.18), and (2.21) gives the system of equations which we solve numerically. These equations can be expressed in matrix form as

$$\begin{pmatrix} \mathbb{I} & 0 & 0 & 0 \\ 0 & \mathbb{I} & 0 & 0 \\ 0 & 0 & \tilde{B}^0 & 0 \\ 0 & 0 & 0 & \tilde{B}^0 \end{pmatrix} \partial_t \begin{pmatrix} \mathbf{A} \\ \mathbf{U} \\ \tilde{\mathbf{V}} \\ \phi \end{pmatrix} + \begin{pmatrix} \tilde{B}^1 & 0 & 0 & 0 \\ 0 & \tilde{B}^1 & 0 & 0 \\ 0 & 0 & \tilde{B}^1 & 0 \\ 0 & 0 & 0 & \tilde{B}^1 \end{pmatrix} \partial_\theta \begin{pmatrix} \mathbf{A} \\ \mathbf{U} \\ \tilde{\mathbf{V}} \\ \phi \end{pmatrix} = \begin{pmatrix} \alpha_0 & 0 & 0 & 0 \\ 0 & \alpha_0 & 0 & 0 \\ 0 & 0 & 0 & 0 \\ 0 & 0 & 0 & \alpha_0 \end{pmatrix} \begin{pmatrix} \mathbf{A} \\ \mathbf{U} \\ \tilde{\mathbf{V}} \\ \phi \end{pmatrix} + \begin{pmatrix} F_{\mathbf{A}} \\ F_{\mathbf{U}} \\ F_{\tilde{\mathbf{V}}} \\ F_\phi \end{pmatrix}, \quad (2.22)$$

$$\partial_t \begin{pmatrix} \alpha \\ \eta \\ A \\ U \\ \phi \end{pmatrix} = \begin{pmatrix} F_\alpha \\ F_\eta \\ A_0 \\ U_0 \\ \phi_0 \end{pmatrix}, \quad (2.23)$$

where

$$\begin{aligned} \mathbf{A} &= (A_0, A_1)^T, \quad \mathbf{U} = (U_0, U_1)^T, \quad \phi = (\phi_0, \phi_1)^T, \\ \tilde{B}^1 &= \begin{pmatrix} 0 & -e^\alpha \\ -e^\alpha & 0 \end{pmatrix}, \quad \tilde{B}^0 = \begin{pmatrix} 1 & 0 \\ 0 & 1 \end{pmatrix}, \quad \tilde{B}^1 = \begin{pmatrix} 0 & -e^\alpha \\ -e^\alpha & 0 \end{pmatrix}, \\ F_{\mathbf{A}} &= (-A_0 - 4A_0U_0 + 4A_1U_1, 0)^T, \quad F_{\mathbf{U}} = \left(\frac{1}{2} + \frac{1}{2}e^{4U}(A_0^2 - A_1^2) + U_0 + \frac{1}{2}\alpha_0, 0 \right)^T, \\ F_\phi &= (\phi_0, 0)^T, \quad F_\alpha = -1 - e^{\frac{3(1+K)}{2}t-2U+2\alpha+2\eta}(K-1)\tilde{\rho}, \\ F_\eta &= -e^{\frac{3(1+K)}{2}t-2U+2\alpha+2\eta}\tilde{\rho} - \frac{1}{4}e^{2t+4U}(A_1^2 + A_0^2) \\ &\quad + \frac{1}{2}\left(-2e^{\frac{3(1+K)}{2}t+2\alpha}(1+K)\tilde{\rho}v_1^2 - 2U_1^2 - \phi_1^2 \right) - U_0^2 - \frac{1}{2}\phi_0^2, \end{aligned}$$

and $\tilde{\mathbf{V}}$, \tilde{B}^0 , \tilde{B}^1 and $F_{\tilde{\mathbf{V}}}$ are as defined above in the preceding section. Furthermore, we note that the momentum constraint (2.13) takes the form

$$\partial_\theta\eta = -e^{3/2(1+K)t}(1+K)\tilde{\rho}v_1\sqrt{e^{2\alpha}(e^{-2U+2\eta} + (v_1)^2)} - \partial_\theta\alpha - \frac{1}{2}e^{2t+4U}A_0\partial_\theta A - 2U_0\partial_\theta U - \phi_0\partial_\theta\phi. \quad (2.24)$$

3. FLRW SOLUTIONS

As discussed in the introduction, the main aim of this article is to study Gowdy symmetric perturbations of FLRW solutions (i.e. spatially homogeneous and isotropic) to the Einstein-Euler-scalar field equations. This requires us to first identify the FLRW solutions. To this end, we observe that a FLRW metric can be recovered from the Gowdy metric (2.6) by setting $\eta = -t$, $U = -\frac{1}{2}t$, and $A = 0$ and assuming that the remaining metric function α depends only on t . This gives a metric of the form

$$g = e^{-t}(e^{2\alpha(t)}dt^2 + d\theta^2 + dy^2 + dz^2).$$

Clearly, this metric ansatz is both spatially homogeneous and isotropic, and hence, if we can find a solution to the Einstein-Euler-scalar field equations of this form it must, by definition, be the FLRW solution. For matter variables $\tilde{\rho}$, v_1 and ϕ , spatial homogeneity and isotropy requires that $v_1 = 0$ and that $\tilde{\rho}$ and ϕ depend only on t . For these choices, the Gowdy-symmetric Einstein-Euler scalar field equations (2.23) simplify to

$$\partial_t\tilde{\rho} = 0, \quad (3.1)$$

$$\partial_t\alpha + e^{\frac{1}{2}(3K+1)t+2\alpha}(K-1)\tilde{\rho} + 1 = 0, \quad (3.2)$$

$$2\phi_0^2 + 4e^{\frac{1}{2}(3K+1)t+2\alpha}\tilde{\rho} - 3 = 0, \quad (3.3)$$

$$2\phi_0^2 + 4\partial_t\alpha + 1 + 4e^{\frac{1}{2}(3K+1)t+2\alpha}K\tilde{\rho} + 1 = 0, \quad (3.4)$$

$$\partial_t\phi_0 - \phi_0\partial_t\alpha - \phi_0 = 0, \quad (3.5)$$

$$\partial_t\phi = \phi_0. \quad (3.6)$$

We begin solving the above system by first noting that (3.1) implies

$$\tilde{\rho} = \frac{1}{\tilde{c}(1+K)}$$

where the constant $\tilde{c} > 0$ can be freely chosen. Next, we integrate (3.2) to obtain

$$\alpha = -\frac{1}{2} \log \left(\frac{4}{3} e^{\frac{3(K-1)}{2}t} \frac{1}{\tilde{c}(K+1)} - 2c_1 \right) - t$$

where c_1 is freely specifiable integration constant. Substituting this into (3.3) and setting $c_1 = -1$, we solve for $\phi_0 = \partial_t \phi$ and integrate the resulting expression while enforcing the initial condition⁸ $\phi|_{t=0} = 0$ to get

$$\phi = \frac{2\sqrt{2}}{\sqrt{3}(1-K)} \left(\sinh^{-1} \left(\sqrt{\frac{3}{2}} \tilde{c}(1+K) e^{\frac{3(1-K)}{4}t} \right) - \sinh^{-1} \left(\sqrt{\frac{3}{2}} \tilde{c}(1+K) \right) \right).$$

It is then straightforward to check that the above expressions for $\tilde{\rho}$, α , and ϕ also satisfy the remaining equations (3.4)-(3.6). From this, we conclude that for each choice of constant $\tilde{c} > 0$, the following defines the FLRW solution of the Einstein-Euler-scalar field equations:

$$\begin{aligned} g &= e^{-t} \left(\frac{-3\tilde{c}e^{-2t}(1+K)}{4e^{\frac{3(K-1)}{2}t} + 6\tilde{c}(1+K)} dt^2 + d\theta^2 + dy^2 + dz^2 \right), \\ \rho &= \frac{1}{\tilde{c}(1+K)} e^{\frac{3(1+K)}{2}t}, \\ v &= \sqrt{\frac{3\tilde{c}e^{-3t}(1+K)}{4e^{\frac{3(K-1)}{2}t} + 6\tilde{c}(1+K)}} dt, \\ \phi &= \frac{2\sqrt{2}}{\sqrt{3}(1-K)} \left(\sinh^{-1} \left(\sqrt{\frac{3}{2}} \tilde{c}(1+K) e^{\frac{3(1-K)}{4}t} \right) - \sinh^{-1} \left(\sqrt{\frac{3}{2}} \tilde{c}(1+K) \right) \right). \end{aligned} \tag{3.7}$$

Remark 3.1. The Einstein-Euler-scalar field FLRW solution has no closed solution in terms of the standard FLRW coordinates⁹ for arbitrary values of K [20]. This can be seen by changing our areal time coordinate to the standard FLRW time, which yields an expression in terms of a hypergeometric function,

$$T = \int \sqrt{\frac{3\tilde{c}e^{-3t}(1+K)}{4e^{\frac{3(K-1)}{2}t} + 6\tilde{c}(1+K)}} dt = -\frac{\sqrt{\frac{2}{3}} e^{-3t} {}_2F_1 \left(1, \frac{1}{2} + \frac{1}{1-K}; \frac{2-K}{1-K}; -\frac{2e^{\frac{3}{2}(K-1)t}}{3\tilde{c}(K+1)} \right)}{3\sqrt{\frac{\tilde{c}(K+1)e^{-3t}}{3\tilde{c}(K+1)+2e^{\frac{3}{2}(K-1)t}}}}.$$

In particular, this expression can not be analytically inverted to obtain a closed solution $t = t(T)$.

4. NUMERICAL RESULTS NEAR FLRW

4.1. Numerical Setup. The numerical method we employ to solve (2.22)-(2.23) in this article is closely related to the one we used in [12] to solve the Gowdy-symmetric Einstein-Euler equations in the expanding direction. Specifically, we use a $[0, 2\pi]$ spatial computational spatial domain that is discretised with an equidistant grid consisting of N grid points, and we employ periodic boundary conditions to enforce the 2π -periodicity of the gravitational and matter fields. Spatial derivatives are discretised using 2nd order central finite differences and time integration is performed using a standard 4th order Runge-Kutta method. As a consequence, our code is second order accurate.

4.1.1. Initial Data. Since we are using the Hamiltonian constraint (2.12) to evolve η , the constraints that our initial data for the system (2.22)-(2.22) must satisfy consist of the momentum constraint (2.24) and the constraints (2.14) and (2.17) that arise from the definition of the first order variables A_1 , U_1 and ϕ_1 . The choice of initial data (4.1) below ensures all these constraints are satisfied initially at $t = 0$. Additionally, we choose the fluid's initial spatial velocity v_1 so that it vanishes at least one point on the initial hypersurface at $t = 0$. This is necessary to generate the tilt-instability that leads to the formation of spikes in the fractional density contrast $\frac{\partial_\theta \rho}{\rho}$ and ultimately blow-up on the big bang singularity at $t = \infty$. Following [12, 38], we ensure that

⁸Only derivatives of ϕ appear in the field equations, hence there is no loss of generality from using this condition to choose our integration constant.

⁹By standard FLRW coordinates, we mean metrics of the form $g = -dT^2 + a(T)^2(dx^2 + dy^2 + dz^2)$.

the spatial fluid velocity v_1 vanishes at $t = 0$ by setting it equal to a sinusoidal function with a small amplitude parameter a . For the remainder of this section, we employ initial data of the form¹⁰

$$\begin{aligned}
\dot{\alpha} &= -\log\left(-a \cos(\theta) + \sqrt{\frac{4}{3(K+1)} + 2}\right), \quad a < \sqrt{\frac{4}{3(K+1)} + 2}, \\
\dot{v}_1 &= a \sin(\theta), \\
\dot{\rho} &= \frac{1}{(K+1)\sqrt{e^{2(\eta-U)} + v_1^2}}, \\
\dot{\eta} &= -(2f-1)c \sin(\theta) - d\left(\frac{3\sqrt{1+K}}{\sqrt{4+6(1+K)}} + b\right) \sin(\theta), \\
\dot{U} &= c \sin(\theta), \\
\dot{U}_0 &= -\frac{1}{2} + f, \\
\dot{\phi}_0 &= \frac{3\sqrt{1+K}}{\sqrt{4+6(1+K)}} + b, \\
\dot{\phi} &= d \sin(\theta), \\
\dot{A}_0 &= 0, \\
\dot{A} &= k \sin(\theta) + b, \\
\dot{A}_1 &= e^\alpha \partial_\theta A, \\
\dot{U}_1 &= e^\alpha \partial_\theta U, \\
\dot{\phi}_1 &= e^\alpha \partial_\theta \phi.
\end{aligned} \tag{4.1}$$

where a, b, c, d, f , and k are constants to be specified. Initial data of this form can be considered as a perturbation of FLRW initial data provided that the constants a, b, c, d, f , and k are chosen sufficiently close to zero. This follows from the fact that setting $a = b = c = d = f = k = 0$ in (4.1) produces homogeneous and isotropic (i.e. FLRW) initial data. If the size of the parameters a, b, c, d, f , and k are too large the system is found to become unstable almost immediately. That is, within a small amount of timesteps the variables develop steep gradients and produce numerical errors. Throughout this section, we focus exclusively on initial data with small amplitudes. In particular, all the plots in this section have been generated with $a = b = c = d = f = k = 0.01$, with the exception of Section 4.1.3 where we set $a = b = c = d = f = k = 0$.

4.1.2. Code Tests. The second order accuracy of our code has been verified with convergence tests involving perturbations of FLRW solutions using resolutions of $N = 200, 400, 800, 1600, 3200$, and 6400 grid points. Following [12], we have estimated the numerical discretisation error Δ by taking the \log_2 of the absolute value of the difference between each simulation and the highest resolution run. The results for v_1 and ϕ are shown¹¹ in Figures 1(a)-1(b) from which the second order convergence is clear.

We can use a similar procedure to measure the level of constraint violation during the evolution of the system. Beginning with the momentum constraint (2.24), we define the quantity

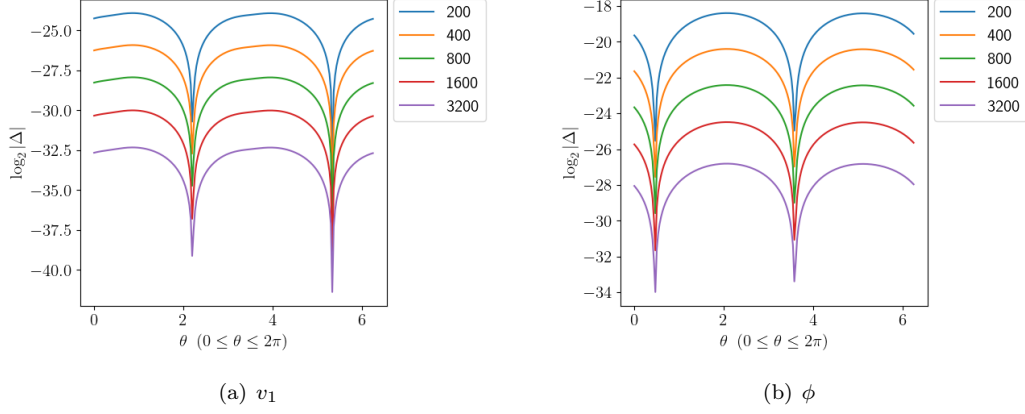
$$C_1 = -\partial_\theta \eta - e^{3/2(1+K)t} (1+K) \tilde{\rho} v_1 \sqrt{e^{2\alpha}(e^{-2U+2\eta} + (v_1)^2)} - \partial_\theta \alpha - \frac{1}{2} e^{2t+4U} A_0 \partial_\theta A - 2U_0 \partial_\theta U - \phi_0 \partial_\theta \phi. \tag{4.2}$$

Clearly, $C_1 = 0$ means that the momentum constraint is identically satisfied. The quantity $\log_2 \|C_1\|_2$ can therefore be understood as the violation error of the momentum constraint as a function of time. In a similar manner, we can also define constraint violation quantities from the definitions of our first order variables A_1 and U_1 , and from the wave equation (2.10) for η as follows

$$\begin{aligned}
C_2 &= A_1 - e^\alpha \partial_\theta A, \\
C_3 &= U_1 - e^\alpha \partial_\theta U, \\
C_4 &= \phi_1 - e^\alpha \partial_\theta \phi, \\
C_5 &= -\partial_{tt} \eta - \frac{1}{4} e^{-2U} \left(4e^{2\alpha+2\eta+\frac{3(1+K)}{2}t} K \tilde{\rho} + e^{2t+6U+2\alpha} (\partial_\theta A)^2 - 4e^{2U+2\alpha} (\partial_\theta U)^2 - 4e^{2U+2\alpha} (\partial_\theta \alpha)^2 \right)
\end{aligned}$$

¹⁰Here we have set the constant $\tilde{c} = 1$.

¹¹We have performed convergence tests for all other variables and confirmed second order convergence. These plots are omitted here for brevity.

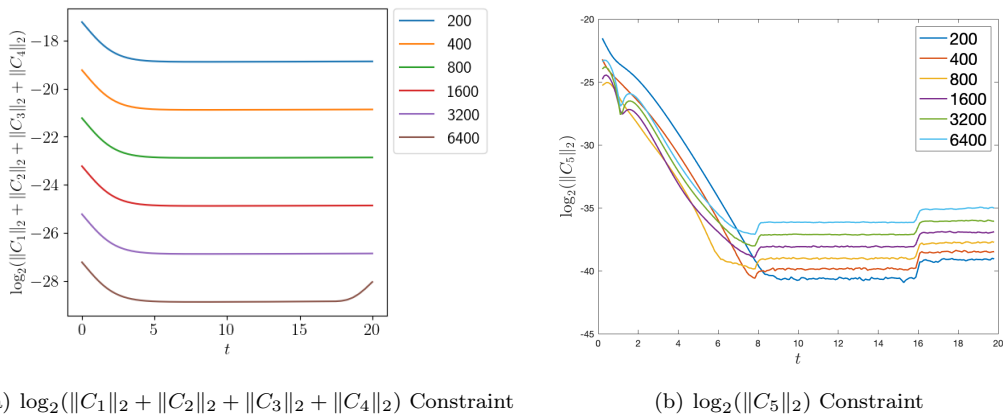

 FIGURE 1. Convergence plots of v_1 and ϕ at $t = 15.07$, $K = 0.1$.

$$\begin{aligned}
 & -4e^{2U+2\alpha}\partial_\theta\alpha\partial_\theta\eta - 2e^{2U+2\alpha}(\partial_\theta\phi)^2 - 4e^{2U+2\alpha}\partial_{\theta\theta}\alpha \\
 & - 4e^{2U}(\partial_t U)^2 - 4e^{2U}\partial_t\alpha\partial_t\eta + 2e^{2U}(\partial_t\phi)^2
 \end{aligned}$$

The second time derivative of η for C_5 is calculated numerically using a fourth order finite difference stencil for the second derivative

$$(\partial_{tt}\eta)_{i,j} = \frac{-\eta_{i-2,j} + 16\eta_{i-1,j} - 30\eta_{i,j} + 16\eta_{i+1,j} - \eta_{i+2,j}}{12(\Delta t)^2}, \quad (4.3)$$

where $\eta_{i,j}$ denotes the value of η at the i^{th} timestep and j^{th} spatial grid point and Δt is the timestep size, while the first time derivatives of α and η in C_5 are calculated using their evolution equations (2.11) and (2.12) respectively. We observe the expected second order convergence for the quantities $\log_2(\|C_1\|_2 + \|C_2\|_2 + \|C_3\|_2 + \|C_4\|_2)$, shown in Figure 2(a). It should be noted that we have been unable to achieve convergence for the constraint quantity $\log_2(\|C_5\|_2)$, plotted in Figure 2(b). Although this constraint does not converge, the overall constraint violation becomes small and approaches the limit of numerical accuracy for a scheme using 2nd order finite difference stencil (approximately 10^{-13}). Even though the constraints are satisfied at the initial time by virtue of our choice of initial data (4.1) so that $C_1 = C_2 = C_3 = C_4 = 0$, we note the numerical values are not exactly zero, even at the initial time $t = 0$, as the derivatives in C_1 , C_2 , C_3 , and C_4 are approximated by finite differences. It should also be noted that, due to our use of the stencil (4.3), the first and last two timesteps in calculating C_5 have been removed from Figure 2(b).


 FIGURE 2. Convergence plots of the constraint quantities, $K = 0.1$. The system was evolved until $t = 20$.

As a further check on the accuracy of the code, we have also compared the size of each individual term in a constraint with the total constraint violation. From this we can conclude that the actual constraint violation is small (as opposed to each individual term being small). To this end we consider C_1 and separate it into six terms as follows:

$$T_1 = -\partial_\theta\eta, \quad (4.4)$$

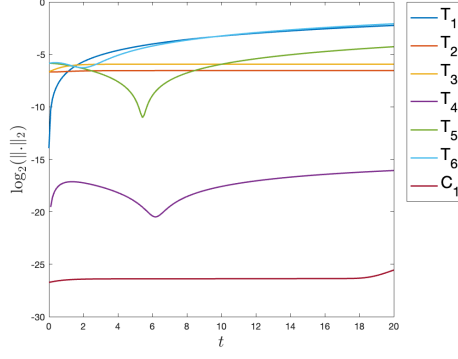


FIGURE 3. Comparison of the L_2 norm of the individual terms in momentum constraint and the combined constraint quantity C_1 . $N = 6400$, $K = 0.1$.

$$T_2 = -e^{3/2(1+K)t}(1+K)\tilde{\rho}v_1\sqrt{e^{2\alpha}(e^{-2U+2\eta} + (v_1)^2)}, \quad (4.5)$$

$$T_3 = -\partial_\theta \alpha, \quad (4.6)$$

$$T_4 = -\frac{1}{2}e^{2t+4U}A_0\partial_\theta A, \quad (4.7)$$

$$T_5 = -2U_0\partial_\theta U, \quad (4.8)$$

$$T_6 = -\phi_0\partial_\theta \phi \quad (4.9)$$

For the constraint violations C_1 to be actually small, we expect that the norm of each individual term (4.4)-(4.9) should be larger than the norm of the total constraint violation C_1 since this indicates that a cancellation among the terms in the sum is occurring. Figure 3 demonstrates that this cancellation is happening for C_1 . We observe similar behaviour for the other constraints, C_2 , C_3 , C_4 , and C_5 . From these observations, we conclude that the constraints are being preserved sufficiently well by our numerical scheme.

4.1.3. Code Validation. A simple way to test the validity of our code is to compare our numerical solution with the exact FLRW solution (3.7). For this convergence test, we employ the following initial data, which is obtained by setting $a = b = c = d = f = k = 0$,

$$\tilde{\rho} = \frac{1}{K+1},$$

$$\alpha = -\log\left(\sqrt{\frac{4}{3(K+1)} + 2}\right),$$

$$\phi_0 = \frac{3\sqrt{1+K}}{\sqrt{4+6(1+K)}},$$

$$U_0 = -\frac{1}{2},$$

$$A = A_1 = A_0 = U = U_1 = \eta = \phi = \phi_1 = v_1 = 0.$$

Due to the homogeneity of the solution, the order of convergence only depends on our time stepping method, which is fourth order accurate. Our scheme displays the expected convergence rate, shown for ϕ_0 in Figure 4.

4.2. Numerical Behaviour.

4.2.1. Asymptotic Behaviour and Approximations. Before we present our numerical results, we first derive the expected asymptotics for the solutions from the evolution equations through a heuristic analysis. In particular, we will justify (1.1); recall that \bar{t} and t are related by (2.5) and that the big bang asymptotics corresponds to the limits $\bar{t} \searrow 0$ and $t \rightarrow \infty$, respectively. To this end, we suppose that, near the singularity, the Einstein-Euler-scalar field system is well-approximated by an FLRW solution of Einstein-scalar field equations. It follows from (3.7) that this metric takes the asymptotic form

$$g = e^{-t}\left(-\frac{1}{2}e^{-2t}dt^2 + d\theta^2 + dy^2 + dz^2\right), \quad (4.10)$$

which corresponds to the metric variables

$$U = -t/2, \quad \eta = -t, \quad \alpha = -t - \log \sqrt{2}, \quad A = 0.$$

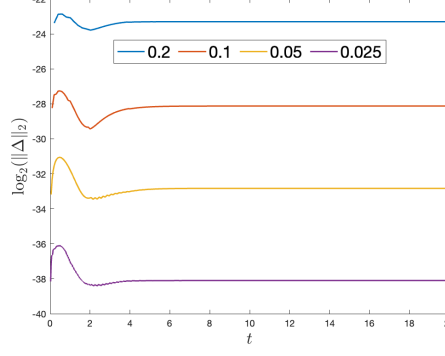


FIGURE 4. Convergence plot of the L_2 norm of $\phi_0 - \phi_0^{\text{exact}}$ for several different values of the timestep Δt . All evolutions used $N = 200$ and $K = 0.2$. The system was evolved until $t = 20$.

Remark 4.1. Employing the time coordinate $T = \frac{\sqrt{2}}{3}e^{-\frac{3}{2}t}$ allows us to express the metric (4.10) in the standard FLRW form

$$g = -dT^2 + \frac{3^{\frac{2}{3}}}{2^{\frac{1}{3}}}T^{\frac{2}{3}}(d\theta^2 + dy^2 + dz^2).$$

As expected for a scalar field solution, the scale factor is proportional to $T^{\frac{1}{3}}$.

Furthermore, we assume that the fluid part of the solution is asymptotically governed by the Euler equations on the background (4.10) with negligible spatial derivative terms. For each spatial point, we therefore have that

$$\tilde{B}^0 = \begin{pmatrix} \frac{K(e^{-t} + (v_1)^2)}{(1+K)\tilde{\rho}} & Kv_1 \\ Kv_1 & (1+K)\tilde{\rho} \end{pmatrix}, \quad \tilde{B}^1 \partial_\theta \tilde{\mathbf{V}} = 0, \quad F_{\tilde{\mathbf{V}}} = \begin{pmatrix} -\frac{K}{2}(v_1)^2 \\ -\frac{3}{2}(1+K)K\tilde{\rho}v_1 \end{pmatrix},$$

and thus, the Euler equations (2.21) reduce to

$$\partial_t \tilde{\mathbf{V}} = -\frac{1}{2} \frac{1}{e^{-t} + (1-K)(v_1)^2} \begin{pmatrix} (1+K)(1-3K)(v_1)^2 \tilde{\rho} \\ K(2(v_1)^2 + 3e^{-t})v_1 \end{pmatrix}. \quad (4.11)$$

It is then straightforward to show that for each spatial point the second equation in (4.11) implies the following implicit solution, cf. (1.1),

$$\frac{e^{t/2}v_1(t)}{(1 + e^t v_1^2(t))^{K/2}} = \frac{\beta(t)}{(1 - \beta^2(t))^{(1-K)/2}} = c e^{-(3K-1)t/2} \quad (4.12)$$

where $c \in \mathbb{R}$ is an integration constant and

$$\beta(t) = \frac{e^{t/2}v_1(t)}{\sqrt{1 + e^t v_1^2(t)}}. \quad (4.13)$$

This solution is only valid for those $t \in \mathbb{R}$ for which $|\beta(t)| < 1$. Recall from (2.7) and (4.10) that the fluid velocity tangent vector field (labelled by the same letter v as the corresponding cotangent vector field in (4.10)) is given by

$$v = -2e^{3t}v_0\partial_t + e^t v_1\partial_\theta = -\sqrt{2}e^{3t/2}v_0e_0 + e^{t/2}v_1e_1 = \frac{1}{\sqrt{1 - \beta^2(t)}}e_0 + \frac{\beta(t)}{\sqrt{1 - \beta^2(t)}}e_1, \quad (4.14)$$

where

$$e_0 = -\sqrt{2}e^{3t/2}\partial_t, \quad e_1 = e^{t/2}\partial_\theta, \quad (4.15)$$

are frame vector fields orthonormal with respect to (4.10).

The implicit solution (4.12) can now be interpreted at each spatial point as follows. If $c = 0$, we have $v_1(t) = \beta(t) = 0$ because the right side of (4.12) is identically zero and we say that the fluid is *orthogonal*. On the other hand, if $c \neq 0$, we consider the three cases: $K \in (1/3, 1]$, $K \in [0, 1/3)$ and $K = 1/3$. Now, if $c \neq 0$ and $K \in (1/3, 1]$, $\beta(t)$ approaches zero as $t \rightarrow \infty$ because the right side of (4.12) approaches zero in the limit $t \rightarrow \infty$. In this case, we refer to the fluid as *asymptotically orthogonal*. Next, if $c \neq 0$ and $K < 1/3$, we have that $\beta^2(t) \rightarrow 1$ since the right side approaches infinity in the limit $t \rightarrow \infty$. Thus, the leading order behaviour of the fluid is a null vector and we call the fluid *asymptotically extremely tilted*. Finally, if $K = 1/3$, then $\beta(t)$ is a non-zero constant and hence the fluid has a non-vanishing asymptotically spatial velocity and we refer to the fluid as *asymptotically tilted*. As mentioned earlier, it is interesting to observe that the limit

$t \rightarrow -\infty$ corresponds to switching the roles of the respective K intervals: the fluid is asymptotically orthogonal if $K < 1/3$ and asymptotically extremely tilted if $K \in (1/3, 1]$.

Using the first equation in (4.11) and (2.20) we conclude that

$$\rho(t) = \rho_0 \exp\left(-\frac{1}{2}(1+K)(1-3K) \int_{t_*}^t \frac{e^s v_1^2(s)}{1+(1-K)e^s v_1^2(s)} ds\right) e^{\frac{3(1+K)}{2}t}, \quad (4.16)$$

where $\rho_0 > 0$ is an integration constant. All of this can be used now to derive the following asymptotics in the limit $t \rightarrow \infty$ from (4.12):

- Orthogonal case ($c = 0$):

$$e^{t/2} v_1(t) = \beta(t) = 0, \quad \rho(t) = O(e^{\frac{3(1+K)}{2}t}). \quad (4.17)$$

- Asymptotically orthogonal case ($c \neq 0$, $K \in (1/3, 1]$):

$$e^{t/2} v_1(t) = O(e^{-(3K-1)t/2}), \quad \beta(t) = O(e^{-(3K-1)t/2}), \quad \rho(t) = O(e^{\frac{3(1+K)}{2}t}). \quad (4.18)$$

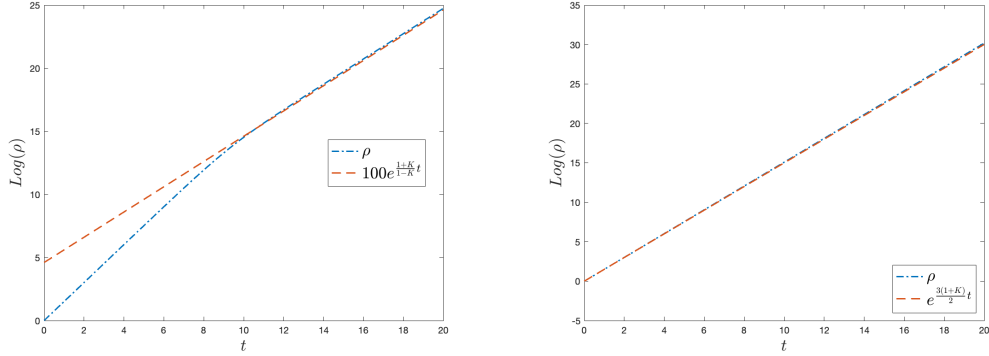
- Asymptotically extremely tilted case ($c \neq 0$, $K \in [0, 1/3)$):

$$e^{t/2} v_1(t) = O(e^{\frac{(1-3K)t}{2(1-K)}}), \quad 1 - \beta^2(t) = O(e^{-\frac{1-3K}{1-K}t}), \quad \rho(t) = O(e^{\frac{1+K}{1-K}t}). \quad (4.19)$$

- Asymptotically tilted case ($c \neq 0$, $K = 1/3$):

$$e^{t/2} v_1(t) = \text{const}, \quad \beta(t) = \text{const}, \quad \rho(t) = O(e^{2t}). \quad (4.20)$$

Our numerical scheme replicates the expected growth rates for all $K \in [0, 1]$. In particular, for $K \in [0, \frac{1}{3})$ we observe the orthogonal growth rate (4.17) near points where v_1 vanishes and the tilted rate (4.19) elsewhere, shown in Figure 5.



(a) ρ at the 334th grid point (Blue) and tilted growth rate (4.19) (Orange) (b) ρ at the 560th grid point (Blue) and orthogonal growth rate (4.17) (Orange)

FIGURE 5. Plot comparing the asymptotic behaviour of ρ with asymptotically orthogonal and extremely tilted growth rates. $N = 1000$, $K = 0.1$.

4.2.2. Behaviour of the Ricci Scalar. We expect to see a curvature singularity in our numerical solutions as $t \rightarrow \infty$, which can be verified by the asymptotic behaviour of the Ricci scalar. Using the trace-reversed Einstein equation the Ricci scalar is given by

$$R = -T = -e^{3/2(1+K)t}(-1 + 3K)\tilde{\rho} + \frac{e^{2U}(\phi_1^2 - \phi_0^2)}{e^{2\alpha+2\eta}},$$

where the T is the trace of the stress-energy tensor. As expected the Ricci curvature blows up as $t \rightarrow \infty$, shown in Figure 6.

4.2.3. Behaviour of the density gradient. The density gradient is, by definition, $\frac{\partial_\theta \rho}{\rho}$. In terms of the re-scaled density (2.20), it is given by

$$\frac{\partial_\theta \rho}{\rho} = \frac{\partial_\theta \tilde{\rho}}{\tilde{\rho}}.$$

As in [12], we observe that the density gradient develops steep gradients and blows up as $t \rightarrow \infty$ for $K \in [0, 1/3)$ if the initial spatial velocity vanishes at at least one point, as shown in Figure 7. On the other hand, for $K \in [1/3, 1]$, we have not observed such fluid spikes, which is consistent with that stability result [14]. This behaviour is shown in Figure 8. The tilt instability is due to the fluid asymptotically approaching two different

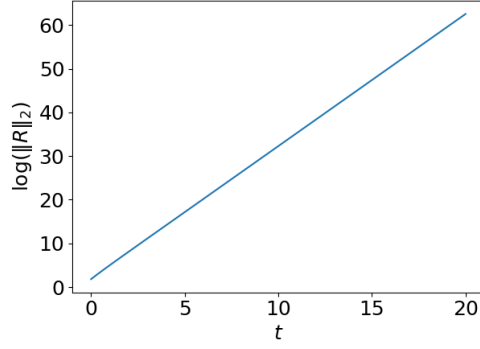


FIGURE 6. The natural logarithm of the L_2 norm of the Ricci scalar. $N = 1000$, $K = 0.1$.

null vectors. This behaviour is particularly apparent when considering the fluid vector in an orthonormal basis. Using the metric (2.6), we obtain the orthonormal frame vectors

$$e_0 = e^{U-\eta-\alpha}\partial_t, \quad e_1 = e^{U-\eta}\partial_\theta,$$

cf. (4.15), for the special case that the metric is (4.10). Following the heuristics from Section 4.2.1, the variable that corresponds to β is

$$\frac{e^{U-\eta}v_1}{\sqrt{1 + e^{2(U-\eta)}v_1^2}}.$$

As the fluid velocity approaches the two null vectors (with opposite tilts), we expect this quantity should approach a step function. This behaviour is confirmed in Figure 9.

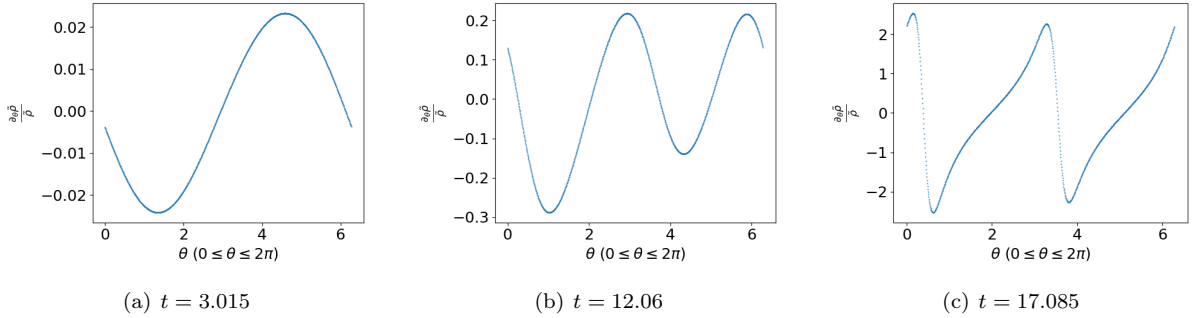


FIGURE 7. Density gradient $\frac{\partial_\theta \rho}{\rho}$ at various times. $N = 1000$, $K = 0.1$.

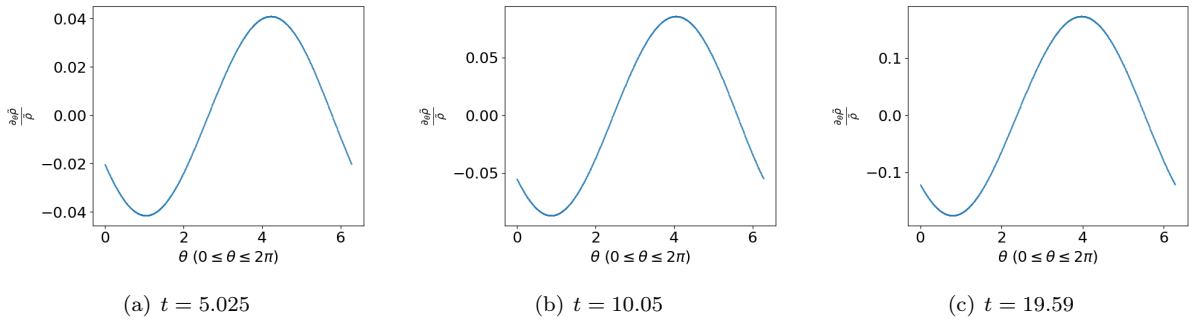


FIGURE 8. Density gradient $\frac{\partial_\theta \rho}{\rho}$ at various times. $N = 1000$, $K = 0.35$.

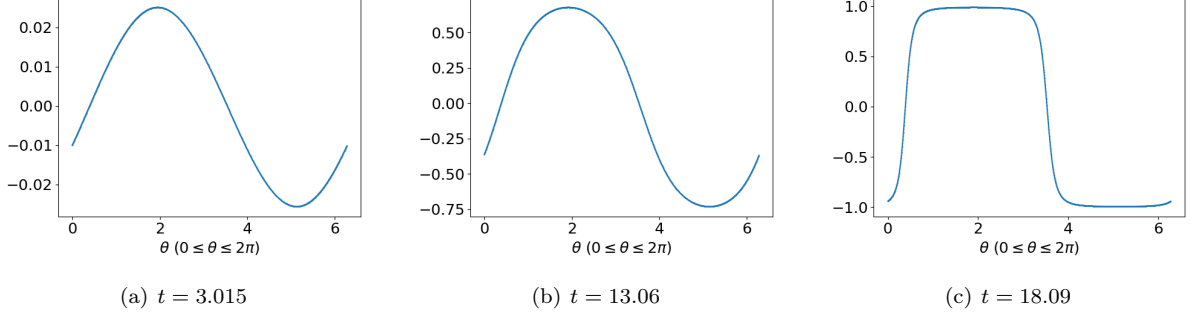


FIGURE 9. $\frac{e^{U-\eta} v_1}{\sqrt{1+e^{2(U-\eta)} v_1^2}}$ at various times. $N = 1000$, $K = 0.1$.

5. LARGE PERTURBATIONS: FLUID AND GRAVITATIONAL SPIKES

5.1. Fluid Spikes for Large Initial Data. In the following, we will consider initial data with large values of the parameters, a , b , c , d , f , and k . As we increase the size of these parameters, our initial data becomes further away from that of the FLRW solution. We find that for suitably large initial data, fluid spikes form for *all values of the parameter K* , shown in Figure 10.

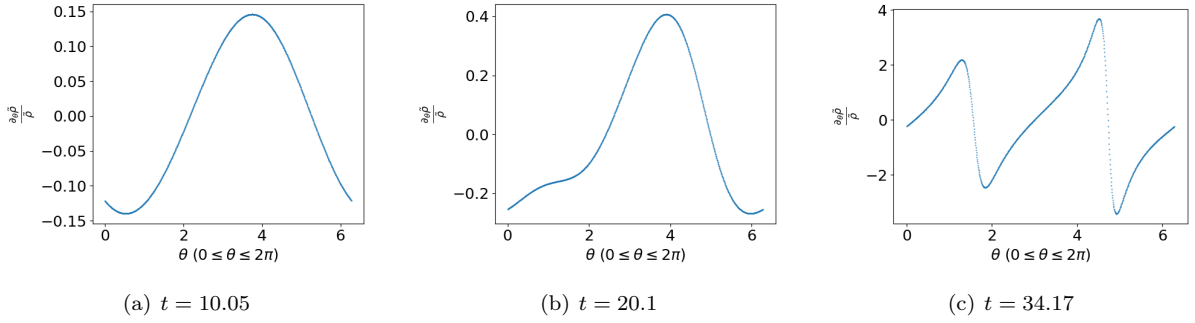


FIGURE 10. Density gradient $\frac{\partial_\theta \rho}{\rho}$ at various times. $N = 1000$, $K = 0.5$, $a = b = c = d = k = 0.01$, $f = 0.5$.

As discussed in the introduction, this is consistent with the behaviour described in [33] where a tilt instability was observed in inhomogeneous cosmological models for $0 < K < 1$. On first appearances, it may seem that these numerical results of this article conflict with the stability of the FLRW big bang singularities for sound speeds $1/3 < K < 1$ that was rigorously established in [14]. However, the stability established in [14] only holds for sufficiently small perturbations of FLRW solutions and, by choosing our initial data suitably large, we have exited the stable regime.

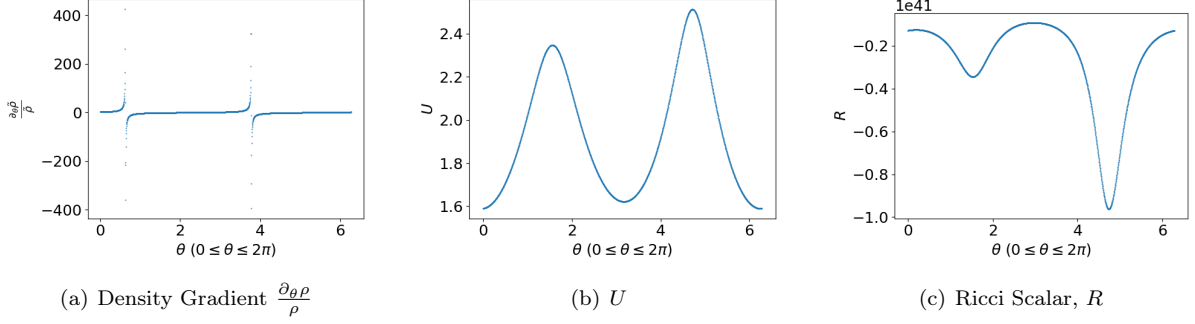
5.2. Gravitational Spikes. We now demonstrate the formation of gravitational spikes in numerical solutions to (2.22)-(2.23) for initial data of the form (4.1) with the parameters a , b , c , d , f , and k set as follows

$$a = b = c = d = k = 0.01, \quad f = 0.5. \quad (5.1)$$

We have been unable to observe spikes in the metric functions for values of a , b , c , d , f , and k which are too close to zero, that is, near a FLRW solution. Following [43], we confirm that spikes produced in our simulations are not coordinate artifacts by observing the behaviour of curvature invariants. If a curvature invariant shows spiky features at the same location as the metric functions, then the spikes are physical rather than gauge¹².

For the choice of parameters (5.3), we observe in our numerical simulations that spikes form at the same location in the fractional density gradient, the metric function U , and the Ricci scalar R as shown in Figure 11. A natural question is whether the fluid spikes in the density gradient are related to the gravitational spikes in U and the Ricci scalar. To test this, we consider initial data for which the fluid velocity crosses zero more than

¹²Physical and gauge spikes are sometimes referred to as ‘true’ and ‘false’ spikes, respectively.

FIGURE 11. Density gradient, U , and the Ricci scalar R at $t = 25.62$. $N = 2000$, $K = 0.2$.

twice. In particular we modify our initial data (4.1) by taking α and v_1 to be

$$v_1 = a \sin(n\theta),$$

$$\dot{\alpha} = -\log \left(-\frac{a}{n} \cos(n\theta) + \sqrt{\frac{4}{3(K+1)} + 2} \right), \quad (5.2)$$

where n is an arbitrary positive integer which determines the number of times v_1 crosses zero. In practice, the value of n corresponds to the number of fluid spikes that initially form in the fractional density gradient. For initial data of the form (5.2), we observe that the spikes in the density gradient form first, followed by gravitational spikes in U and the Ricci scalar at the same locations. At late times, we always observe two of the fractional density gradient spikes grow more rapidly than the others, which overwhelms the resolution of our simulations. These larger spikes dominate our plots at late times (i.e. near the big bang singularity), which we suspect masks ‘small’ scale features that are related to the other smaller fractional density gradient spikes. This behaviour is demonstrated in Figures 12(a) - 12(d). In particular, it is clear from Figure 12(d) that our resolution is insufficient to capture any small scale features of the density gradient near the big bang singularity. To generate these plots, we have used the following choice of parameters

$$b = c = d = k = 0.01, \quad a = 0.1, \quad f = 0.5, \quad \text{and} \quad n = 4, \quad (5.3)$$

in our initial data. It should be noted that while increasing the size of a is not necessary to generate multiple fluid spikes, it makes the smaller spikes more apparent before they are overwhelmed by the dominant spikes at late times.

6. DISCUSSION

In this article, we have numerically simulated Gowdy-symmetric, nonlinear perturbations of FLRW solutions to the Einstein-Euler-scalar field equations over the full sound speed parameter range $0 \leq K \leq 1$ in the contracting direction. For $K \in (1/3, 1]$, we observe numerically that sufficiently small perturbations of FLRW solutions are stable towards the past (contracting direction) and terminate in a spacelike big bang singularity in agreement with the analytic results obtained in [14, 47]. For these solutions, all suitably normalised gravitational and matter fields converge monotonically to limits on the big bang singularity. We also observe similar stable behaviour for $K = 1/3$, but as discussed above, a more thorough investigation is required to be confident that we are integrating long enough to resolve the asymptotic behaviour of solutions. On the other hand, for $K \in [0, 1/3)$, we observe numerically that small perturbations of the FLRW solutions for which the spatial fluid velocity vanishes somewhere on the initial hypersurface are unstable towards the past. These solutions still terminate in the past at a spacelike big bang singularity, but now the fluid develops a fluid tilt-instability that manifests as sharp features (spikes) that develop in the fractional density gradient $\frac{\partial_\theta \rho}{\rho}$ and ultimately lead to blow-up of this quantity at a finitely many spatial points on the big bang singularity. Interestingly, a similar fluid tilt-instability in the expanding direction (to the future) was predicted by Rendall [42] and observed numerically in [12]. We have also observed that for initial data suitably far away from that of the FLRW solution, gravitational spikes form in the metric functions as well as fluid spikes for all $K \in [0, 1]$. While it appears from the numerical simulations that the gravitational spikes are induced by the fluid spikes, more investigation is required to understand the precise relationship. We plan on investigating this further in future work. The results of this article suggest several interesting topics for future research. The obvious first step is to remove the Gowdy symmetry assumption and study the fluid tilt-instability that develops in small perturbations of FLRW solutions for $K \in [0, 1/3)$ without any additional symmetry assumptions. Additionally,

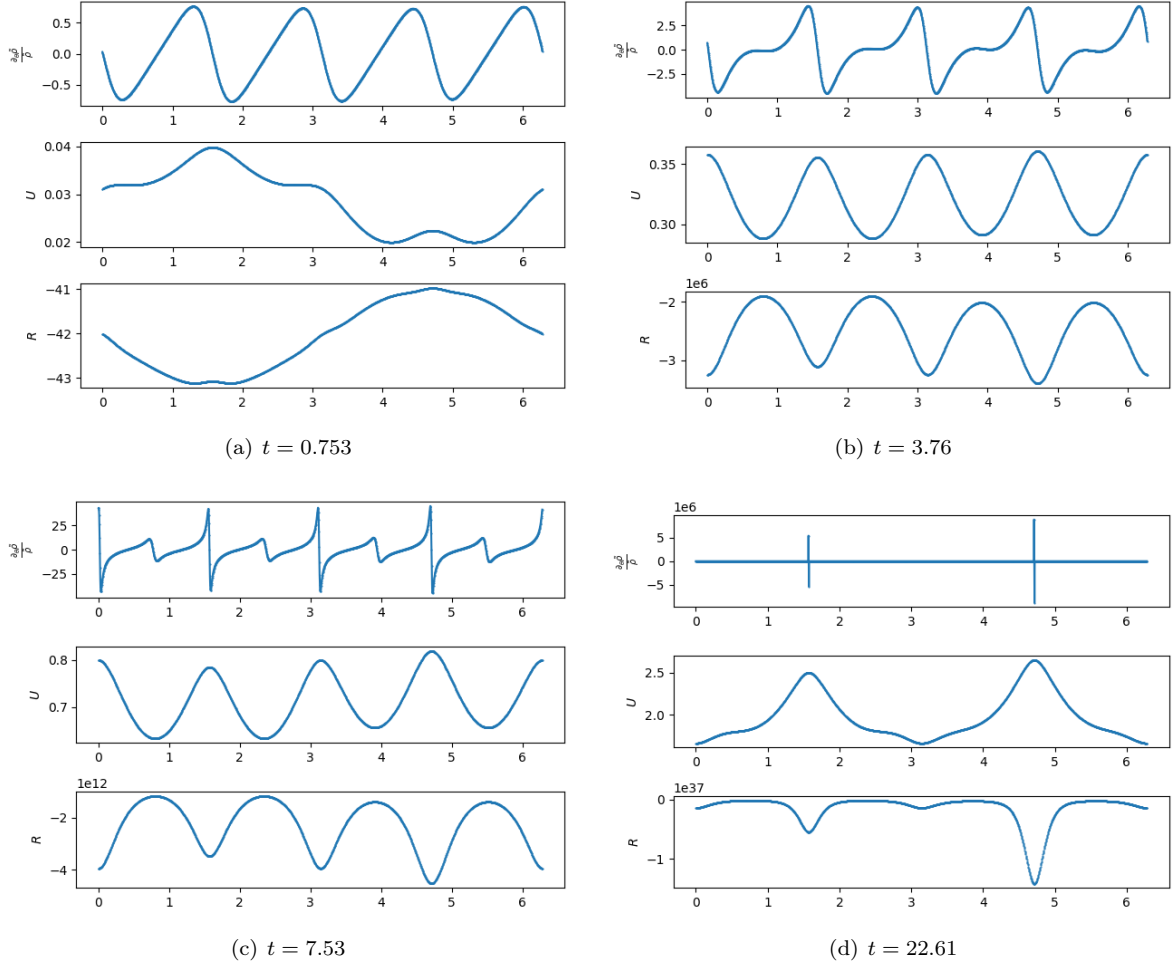


FIGURE 12. Density gradient $\frac{\partial \rho}{\partial \rho}$ (top), U (middle), and the Ricci scalar R (bottom) at various times. $N = 2000$, $K = 0.1$.

it would be interesting to further study the connection between dynamics of the Einstein-Euler system with positive cosmological constant towards the future with the Einstein-Euler-scalar field system towards the past.

REFERENCES

1. E. Ames, F. Beyer, J. Isenberg, and P. G. LeFloch, *A class of solutions to the Einstein equations with AVTD behavior in generalized wave gauges*, J. Geom. Phys. **121** (2017), 42–71.
2. P. Amorim, C. Bernardi, and P.G. LeFloch, *Computing Gowdy spacetimes via spectral evolution in future and past directions*, Class. Quantum Grav. **26** (2009), 025007.
3. J.M. Bardeen, P.J. Steinhardt, and M.S. Turner, *Spontaneous Creation of Almost Scale - Free Density Perturbations in an Inflationary Universe*, Phys. Rev. D **28** (1983), 679.
4. V. A. Belinskii, I. M. Khalatnikov, and E. M. Lifshitz, *Oscillatory approach to a singular point in the relativistic cosmology*, Adv. Phys. **19** (1970), no. 80, 525–573.
5. B.K. Berger, *Why solve the hamiltonian constraint in numerical relativity?*, Gen. Rel. Grav. **38** (2006), 625–632.
6. B.K. Berger and D. Garfinkle, *Phenomenology of the Gowdy universe on $T^3 \times R$* , Phys. Rev. D **57** (1998), 4767–4777.
7. B.K. Berger, J. Isenberg, and M. Weaver, *Oscillatory approach to the singularity in vacuum spacetimes with T^2 isometry*, Phys. Rev. D **64** (2001).
8. B.K. Berger and V. Moncrief, *Numerical investigation of cosmological singularities*, Phys. Rev. D **48** (1993), no. 10, 4676–4687.
9. F. Beyer and J. Hennig, *Smooth Gowdy-symmetric generalized Taub-Nut solutions*, Class. Quantum Grav. **29** (2012), 245017.
10. F. Beyer and P. G. LeFloch, *Second-order hyperbolic Fuchsian systems and applications*, Class. Quantum Grav. **27** (2010), no. 24, 245012.
11. ———, *Self-gravitating fluid flows with Gowdy symmetry near cosmological singularities*, Commun. Part. Diff. Eq. **42** (2017), no. 8, 1199–1248.
12. F. Beyer, E. Marshall, and T.A. Oliynyk, *Future instability of flrw fluid solutions for linear equations of state $p = K\rho$ with $1/3 < K < 1$* , Phys. Rev. D **107** (2023), 104030.
13. F. Beyer and T.A. Oliynyk, *Localized Big Bang Stability for the Einstein-Scalar Field Equations*, Arch. Rat. Mech. Anal. **248** (2024), 3.

14. F. Beyer and T.A. Oliynyk, *Past stability of FLRW solutions to the Einstein-Euler-scalar field equations and their big bang singularities*, Beijing J. of Pure and Appl. Math. **1** (2024), 515–637.
15. Florian Beyer and Philippe G. LeFloch, *A numerical algorithm for Fuchsian equations and fluid flows on cosmological space-times*, J. Comput. Phys. **431** (2021), 110145.
16. P.T. Chruściel, *On space-times with $U(1) \times U(1)$ symmetric compact Cauchy surfaces*, Ann. Phys. **202** (1990), no. 1, 100–150.
17. A. A. Coley and W. C. Lim, *Generating matter inhomogeneities in general relativity*, Phys. Rev. Lett. **108** (2012), 191101.
18. A A Coley and W C Lim, *Spikes and matter inhomogeneities in massless scalar field models*, Classical and Quantum Gravity **33** (2016), no. 1, 015009.
19. D. Fajman and L. Urban, *Cosmic Censorship near FLRW spacetimes with negative spatial curvature*, preprint [arXiv:2211.08052], 2022.
20. Valerio Faraoni, Sonia Jose, and Steve Dussault, *Multi-fluid cosmology in einstein gravity: analytical solutions*, General Relativity and Gravitation **53** (2021), no. 12.
21. G. Fournodavlos, *Future dynamics of FLRW for the massless-scalar field system with positive cosmological constant*, J. Math. Phys. **63** (2022), 032502.
22. G. Fournodavlos, I. Rodnianski, and J. Speck, *Stable Big Bang formation for Einstein’s equations: The complete sub-critical regime*, J. Amer. Math. Soc. **36** (2023), 827–916.
23. H. Friedrich, *Sharp asymptotics for Einstein- λ -dust flows*, Comm. Math. Phys. **350** (2017), 803 – 844.
24. R.H. Gowdy, *Vacuum spacetimes with two-parameter spacelike isometry groups and compact invariant hypersurfaces: Topologies and boundary conditions*, Ann. Phys. **83** (1974), 203–241.
25. H. Oude Groeniger, O. Petersen, and H. Ringström, *Formation of quiescent big bang singularities*, 2023, preprint [arXiv:2309.11370].
26. A.H. Guth, *Inflationary universe: A possible solution to the horizon and flatness problems*, Phys. Rev. D **23** (1981), 347–356.
27. M. Hadžić and J. Speck, *The global future stability of the FLRW solutions to the Dust-Einstein system with a positive cosmological constant*, J. Hyper. Differential Equations **12** (2015), 87–188.
28. S. W. Hawking and G. F. R. Ellis, *The large scale structure of space-time*, first ed., Cambridge University Press, 1973.
29. J. Isenberg and V. Moncrief, *Asymptotic behavior of the gravitational field and the nature of singularities in Gowdy spacetimes*, Ann. Phys. **199** (1990), 84–122.
30. S. Kichenassamy and A. D Rendall, *Analytic description of singularities in Gowdy spacetimes*, Class. Quantum Grav. **15** (1998), no. 5, 1339–1355.
31. P.G. LeFloch and A.D. Rendall, *A global foliation of Einstein-Euler spacetimes with Gowdy-symmetry on T^3* , Arch. Rat. Mech. **201** (2011), no. 3, 841–870.
32. E. M. Lifshitz and I. M. Khalatnikov, *Investigations in relativistic cosmology*, Adv. Phys. **12** (1963), no. 46, 185–249.
33. W C Lim and A A Coley, *General relativistic density perturbations*, Classical and Quantum Gravity **31** (2013), no. 1, 015020.
34. W.C Lim, L. Andersson, D. Garfinkle, and F. Pretorius, *Spikes in the mixmaster regime of G_2 cosmologies*, Phys. Rev. D **79**.
35. C. Liu and T.A. Oliynyk, *Cosmological Newtonian limits on large spacetime scales*, Commun. Math. Phys. **364** (2018), 1195–1304.
36. ———, *Newtonian limits of isolated cosmological systems on long time scales*, Annales Henri Poincaré **19** (2018), 2157–2243.
37. C. Lübbe and J. A. Valiente Kroon, *A conformal approach for the analysis of the non-linear stability of radiation cosmologies*, Ann. Phys. **328** (2013), 1–25.
38. E. Marshall and T.A. Oliynyk, *On the stability of relativistic perfect fluids with linear equations of state $p = K\rho$ where $1/3 < K < 1$* , Lett. Math. Phys. **113** (2023), 102.
39. T. A. Oliynyk, *Future stability of the FLRW fluid solutions in the presence of a positive cosmological constant*, Commun. Math. Phys. **346** (2016), 293–312; see the preprint [arXiv:1505.00857] for a corrected version.
40. T.A. Oliynyk, *On the fractional density gradient blow-up conjecture of Rendall*, 2023, preprint [arXiv:2310.19184].
41. A. D Rendall, *Fuchsian analysis of singularities in Gowdy spacetimes beyond analyticity*, Class. Quantum Grav. **17** (2000), no. 16, 3305–3316.
42. A. D. Rendall, *Asymptotics of solutions of the Einstein equations with positive cosmological constant*, Ann. Henri Poincaré **5** (2004), no. 6, 1041–1064.
43. A.D. Rendall and M. Weaver, *Manufacture of Gowdy spacetimes with spikes*, Class. Quantum Gravity **18** (2001), no. 15, 2959–2975.
44. H. Ringström, *Strong cosmic censorship in T^3 -Gowdy spacetimes*, Ann. Math. **170** (2009), no. 3, 1181–1240.
45. I. Rodnianski and J. Speck, *The stability of the irrotational Euler-Einstein system with a positive cosmological constant*, J. Eur. Math. Soc. **15** (2013), 2369–2462.
46. ———, *A regime of linear stability for the Einstein-scalar field system with applications to nonlinear Big Bang formation*, Ann. Math. **187** (2018), 65–156.
47. ———, *Stable Big Bang formation in near-FLRW solutions to the Einstein-scalar field and Einstein-stiff fluid systems*, Sel. Math. New Ser. **24** (2018), 4293–4459.
48. ———, *On the nature of Hawking’s incompleteness for the Einstein-vacuum equations: The regime of moderately spatially anisotropic initial data*, J. Eur. Math. Soc. **24** (2022), 167–263.
49. J. Speck, *The nonlinear future-stability of the FLRW family of solutions to the Euler-Einstein system with a positive cosmological constant*, Selecta Mathematica **18** (2012), 633–715.
50. J. Speck, *The Maximal Development of Near-FLRW Data for the Einstein-Scalar Field System with Spatial Topology \mathbb{S}^3* , Commun. Math. Phys. **364** (2018), 879–979.

DEPT OF MATHEMATICS AND STATISTICS, 730 CUMBERLAND ST, UNIVERSITY OF OTAGO, DUNEDIN 9016, NEW ZEALAND
Email address: `florian.beyer@otago.ac.nz`

SCHOOL OF MATHEMATICS, 9 RAINFOREST WALK, MONASH UNIVERSITY, VIC 3800, AUSTRALIA
Email address: `elliott.marshall@monash.edu`

SCHOOL OF MATHEMATICS, 9 RAINFOREST WALK, MONASH UNIVERSITY, VIC 3800, AUSTRALIA
Email address: `todd.oliynyk@monash.edu`